Supplementary information for

Synergistic regulation of crystallization and buried-interface in $Cs_xFA_{1-x}PbI_3$ perovskite photovoltaics using a multifunctional sulfonyl–ammonium additive

Sanwan Liu,†*[ab] Yifei Xu,†[a] Tianyin Miao,†[a] Qian Liu,†[c] Likai Zheng,†[d] Rui Chen,[a] Jianan Wang,[a] He Zhu,[a] Zhengtian Tan,[a] Ziming Yin,[a] Yan Zhao,[e] Wei Chen,*[ab] Michael Grätzel*[d] and Zonghao Liu*[ab]

[a]*Wuhan National Laboratory for Optoelectronics (WNLO), Huazhong University of Science and Technology (HUST), Wuhan 430074, China.*

[b]*Optics Valley Laboratory, Hubei, 430074, China.*

[c]*Hoffmann Institute of Advanced Materials, Shenzhen Polytechnic University, 7098 Liuxian Boulevard, Shenzhen, 518055 China.*

[d]*Laboratory of Photonics and Interfaces, École Polytechnique Fédérale de Lausanne, Lausanne, Switzerland.*

[e]*College of Materials Science and Engineering, Sichuan University, Chengdu, 610065, P. R. China.*

†These authors contributed equally to this work.

*Corresponding authors: liusanwan@hust.edu.cn; wnlochenwei@hust.edu.cn; michael.graetzel@epfl.ch; liuzonghao@hust.edu.cn.

Experimental Section

Materials

Lead iodide (PbI_2), formamidinium iodide (FAI), cesium bromide (CsBr), [6,6]-phenyl-C_{61}-butyric acid methyl ester ($PC_{61}BM$), Tin (IV) oxide 15% in water and 2,2′,7,7′-tetrakis(N,N-di-p-methoxyphenylamine)-9,9′-spirobifluorene (Spiro-MeOTAD), and nickel oxide (NiO_x) nanoparticles were purchased from Advanced Election Technology Co., Ltd. Piperazinium diiodide (PDI), methylammonium iodide (MAI), methylamine hydrochloride (MACl), [4-(3,6-dimethyl-9H-carbazol-9-yl)butyl]phosphonic acid (Me-4PACz), cesium iodide (CsI), and bathocuproine (BCP) were obtained from TCI Japan. 2-aminoethylmethylsulfone hydrochloride (AEMS), [2-(ethylsulfonyl)ethyl]amine hydrochloride (ESEA), and 4,4',4''-nitrilotribenzoicacid (NA) were purchased from Aladdin Biochemical Technology Co., bistrifluoromethanesulfonimide lithium salt (Li-TFSI), 4-tert-butylpyridine (*t*-BP), and C_{60} were purchased from Xi'an Yuri Solar Co., Ltd. All solvents were purchased from Sigma-Aldrich.

Preparation of NiO_x layer

The concentration of NiO_x nanoparticle ink was 10 mg mL^{-1} in a mixed solution of deionized water and IPA (3:1, vol/vol). The NiO_x layer was formed by spin-coating NiO_x nanoparticle ink onto the ITO substrate at 3,000 rpm for 20 s, followed by annealing at 110 °C for 10 min in an air environment, and then transferred to an N_2-filled glovebox.

Preparation of the SAM layer

The solutions of Me-4PACz and NA with the same concentration (1 mmol L^{-1} in absolute ethanol) were mixed in a molar ratio of 3:1, then were spin-coated on NiO_x at 3,000 rpm for 20 s, followed by annealing at 100 °C for 10 min to form a mixed SAM layer in a N_2-filled glovebox.

Preparation of perovskite precursors and films for small-area PSCs

For the composition $FA_{0.95}Cs_{0.05}PbI_3$, the 1.6 M perovskite precursor solution was prepared by mixing FAI, CsI, and PbI_2 in DMF:DMSO = 5:1 (vol/vol) mixed solvent subject to the stochiometric ratio. Additional 3 mol% PbI_2 and 20 mol% MACl were added to the precursor for better crystallization and perovskite phase transformation. For the perovskite solution with AEMS/ESEA agents, AEMS (or ESEA) (1 mg mL^{-1}) powders were directly added into the perovskite precursor solution. The perovskite precursor (60 μL) was spin-coated at 5,000 rpm for 50 s (5 s acceleration to 5,000 rpm). Chlorobenzene (200 μL) was dropped on the film at 20 s before the end of the spinning. The wet film was immediately annealed at 100 °C for 45 min in a N_2-filled glovebox.

PSCs fabrication

For the rigid devices, the ITO glass substrates were sequentially washed with detergent, deionized water, alcohol, and IPA for 20 min in an ultrasonic bath, respectively, followed by ultraviolet ozone treatment for 20 min. NiO_x, SAMs, and the perovskite layer were sequentially fabricated following the aforementioned procedures. For surface passivation, 4–6 mg of PDI was first dissolved in 3.6 mL of IPA, followed by the addition of a small amount of NMP (NMP:IPA = 1:200, v/v). The resulting solution was spin-coated onto the perovskite films at 5,000 rpm for 30 s and subsequently annealed at 100 °C for 3 min. Then, the PCBM solution (20 mg mL^{-1}, in chlorobenzene) was spin-coated on the perovskite film as an electron transport layer at 3,000 rpm for 20 s and annealed at 70 °C for 10 min. Sequentially, the saturated solution of BCP in methanol was dynamically spin-coated on the PCBM layer at 6,000 rpm for 30 s and annealed at 70 °C for 10 min. Finally, a 100 nm Ag electrode was evaporated with a controlled evaporation rate of 0.1 Å s^{-1} to 0.5 Å s^{-1}, respectively, in a vacuum chamber ($< 3 \times 10^{-4}$ Pa). For flexible small-area PSCs, the fabrication procedures were identical to those of rigid devices, except for the use of ITO/PET substrates. For n-i-p PSCs, the FTO substrate was spin-coated with a thin layer of SnO_2 nanoparticle film (2.67%, diluted by water) at 4000 rpm for 30 seconds. Subsequent annealing was performed at 150 °C for 30 min in ambient air, after which the substrates were transferred to a nitrogen-filled glove box. The perovskite layer and passivation layer were prepared following the same procedure as described above. Then, the spiro-OMeTAD precursor (72.3 mg spiro-OMeTAD, 30 μL 4-tert-butylpyridine solution, and 35 μL Li-TFSI in 1 mL chlorobenzene) was deposited at 3000 rpm for 30 s with 1500 rpm s^{-1}. Finally, a 100 nm Au electrode was evaporated with a controlled evaporation rate of 0.1 Å s^{-1} to 0.5 Å s^{-1}, respectively, in a vacuum chamber ($< 3 \times 10^{-4}$ Pa).

PSMs fabrication

For modules with dimensions of 5 × 5 cm, the cleaned glass/FTO substrates were first laser scribed to form P1 lines-isolated cell units, using a 532 nm nanosecond beam with a power of 2 W. The PSMs' fabrication process was identical to that of the small-area cells. After depositing the BCP layer, the module was re-etched to form P2 lines with a power of 0.3 W. Finally, it formed effective monolithically interconnected modules by scribing the Cu electrode using a power of 0.3 W to form P3 lines. P4 is an etching procedure for cleaning the edge of the modules; the laser used in P4 is the same as in P1. The series interconnection of modules was realized through P1, P2, and P3 lines. Pattern of the lines used a laser scribing system with a wavelength of 532 nm, a frequency of 50 KHz, a power of 7.2 W, and a laser processing speed of 100 mm s^{-1}. The widths of P1, P2, and P3 are 50, 100, and 60 μm, respectively.

Stability tests

The Bi/Cu (20 nm/120 nm) bilayer electrode was used instead of the Ag electrode for stability tests. The encapsulation of the PSC was processed according to our previous report.[1] Details of the operational stability tests can be found in our previous work.[2] For the heat test (85 °C, N_2), we put the unencapsulated devices on the hot plate at 85 °C in the N_2 glovebox and measured the PCEs periodically after the devices cooled to room temperature.

Characterization

^{1}H-NMR spectra were detected at room temperature using a 600 MHz Bruker AVANCE III-400 NMR spectrometer. Co., Japan). The FTIR spectra were obtained by a VERTEX

70 FTIR microscope (Bruker Co., Germany). Ultraviolet-visible (UV-vis) absorption spectra were obtained using a UV-Vis spectrometer (PerkinElmer Co., USA). TGA analysis was performed using TGA8000 (PerkinElmer Co., USA) under dry air conditions with a heating rate of 10 °C min^{-1}. The steady-state PL spectra were recorded by the Edinburgh FLS920 fluorescence spectrometer (Edinburgh Co., UK) with an excitation source wavelength of 532 nm. TRPL spectra were measured by time-correlated single-photon counting (TCSPC) with a 410 nm beam source and 5 MHz repetition rate. The transient decay curves were empirically fitted using a bi-exponential equation of $I_{(t)} = A_1 \exp(-(t\text{-}x_0)/\tau_1) + A_2 \exp(-(t\text{-}x_0)/\tau_2) + y_0$, where the fast decay component (τ_1) is mainly attributed to trap-assisted recombination at defects or interfaces (first-order-like process), while the slow component (τ_2) is assigned to band-to-band radiative recombination for free carriers in the perovskite bulk (second-order-like process). The top-view and bottom-view images of the samples were obtained by a field-emission SEM (FEI NOVA NanoSEM 450). In-situ GIWAXS characterizations with the incidence angle of 0.5° were performed at BL14B and 20U2 RSoXS beamlines at the Shanghai Synchrotron Facility and BL17B1 beamlines at the National Facility for Protein Science in Shanghai, China. In situ PL spectra (Fig. 2D-2F) were recorded on a Du-100 dynamic spectrometer system (Puguangweishi Co. Ltd) in an N_2-filled glovebox. In situ PL spectra (Fig. 4G and 4H) were obtained by a home-built setup utilizing the ProSp-Micro-MVIS microspectroscopy system (Hangzhou SPL Photonics Co., Ltd.). The samples were excited with a 405 nm laser at an excitation intensity of 1000 mW cm^{-2}, and the data were collected by a QE-Pro monochromator from Ocean Optics. The GIXRD patterns were conducted in the air by using a Rigaku Smartlab with Cu Kα radiation in the 2θ range from 30.6° to 32.6° (incident angle: 0.2°). Fluorescence lifetime imaging microscopy (FLIM) was measured using FLIM300 (Dalian Chuangrui Spectral Technology Co., Ltd). The ultraviolet photoelectron spectroscopy (UPS) data were obtained using an AXIS-ULTRA DLD-600W Ultra spectrometer (Kratos Co., Japan) equipped with a non-monochromatic He Iα photon source (hv = 21.22 eV). X-ray photoelectron spectroscopy (XPS) system (Thermo ESCALAB 250XI) equipped with a monochromatic Al Kα X-ray source (1486.6 eV) operating at 100 W

(Worcestershire, UK). TOF-SIMS measurements were conducted using a TOF-SIMS V instrument (IONTOF GmbH, 170 Cameca IMS 4F). The trap density of state (tDOS) was estimated from thermal admittance spectroscopy measurements based on the method reported elsewhere.[3] The *J–V* curves of the devices were recorded with a black mask with an active area of 0.0586 cm^2 (for small-area PSCs) using a Keithley 2400 SourceMeter and a solar simulator (Oriel, model 9119) under AM 1.5G one sun illumination. The light intensity was adjusted with a reference silicon solar cell (KG3, Enlitech). During the *J–V* measurement, the scanning speed and dwell time for both forward and reverse scans were 0.02 V s^{-1} and 100 ms, respectively. No device preconditioning was performed prior to testing. The devices were tested in ambient air conditions. The external quantum efficiency (EQE) spectra were measured under DC mode using an EQE system (Saifan) with monochromatic light of 1×10^{16} photons cm^{-2}. The transient photovoltage (TPV) measurement was obtained by a Zennium electrochemistry workstation (Zahner, Germany). The PL quantum yield (PLQY) of the corresponding film was measured using a QuantaMaster 8000 (HORIBA, Canada) with a 405 nm laser to photoexcite the samples placed in an integrating sphere. The laser's intensity was calibrated by adjusting the power when it produced a 1-sun-equivalent current density from the devices under J_{SC} conditions.

DFT calculations

Density functional theory (DFT) calculations were performed by using the Vienna ab initio simulation package (VASP),[4,5] using the planewave basis with energy cutoff of 400 eV, the projector augmented wave (PAW) potentials.[6] The generalized gradient approximation with the function of Perdew–Burke–Ernzerhof (GGA-PBE) was applied to describe the exchange-correlation function.[7,8] Grimme's semiempirical DFT-D3 scheme of dispersion correction was adopted to describe the van der Waals (vdW) interactions.[9] The convergence criteria of the residual Hellmann–Feynman force and energy during structure optimization were set to 0.03 eV Å^{-1} and 10^{-5} eV, respectively. The $FAPbI_3$ (100) surface is modelled by a slab consisting of seven atomic layers and a vacuum gap of 30 Å. The bottom two atomic layers in the slab are fixed during structural relaxation. The binding energy of the ligand with the $FAPbI_3$ surface is defined as $E_b = E_{(slab@ligand)} – E_{(slab)} – E_{(ligand)}$. The electrostatic potentials of the ligands were calculated in DMol3 code[10,11] at the m-GGA/M06-L level.[12]

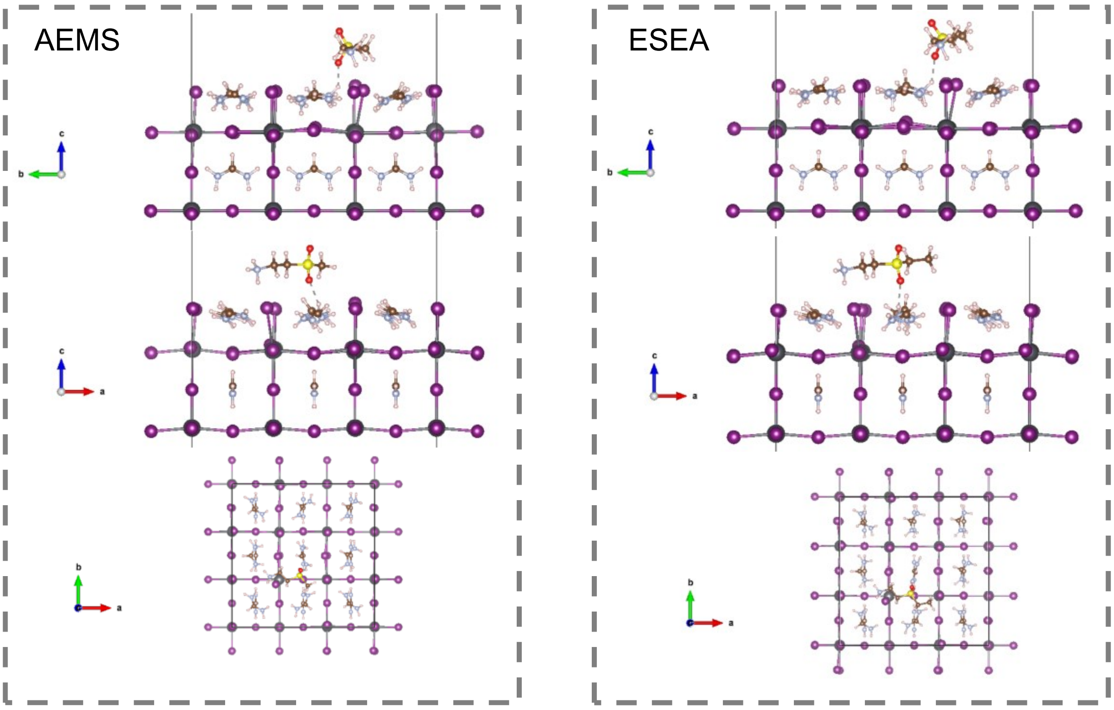

Fig. S1 Atomic structures of the perovskite surface (FAI termination) with AEMS and ESEA ligands in parallel orientation. For each case, front, side, and top views are provided.

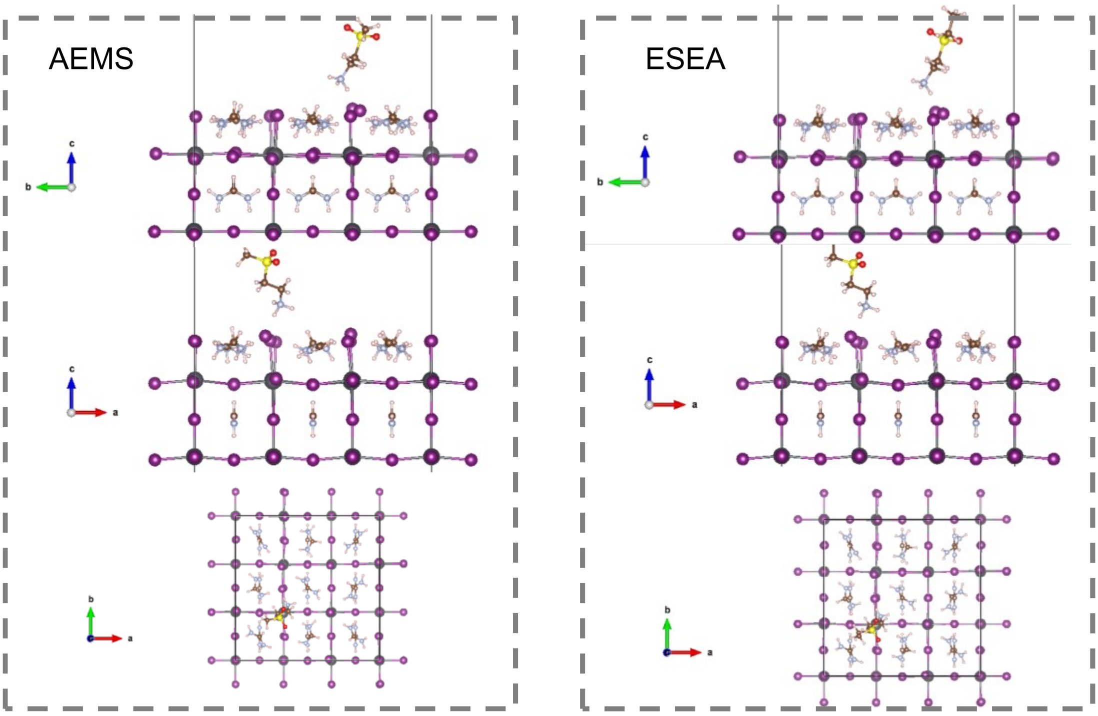

Fig. S2 Atomic structures of the perovskite surface (FAI termination) with AEMS and ESEA ligands in vertical orientation (-NH_3^+ toward the surface). For each case, front, side, and top views are provided.

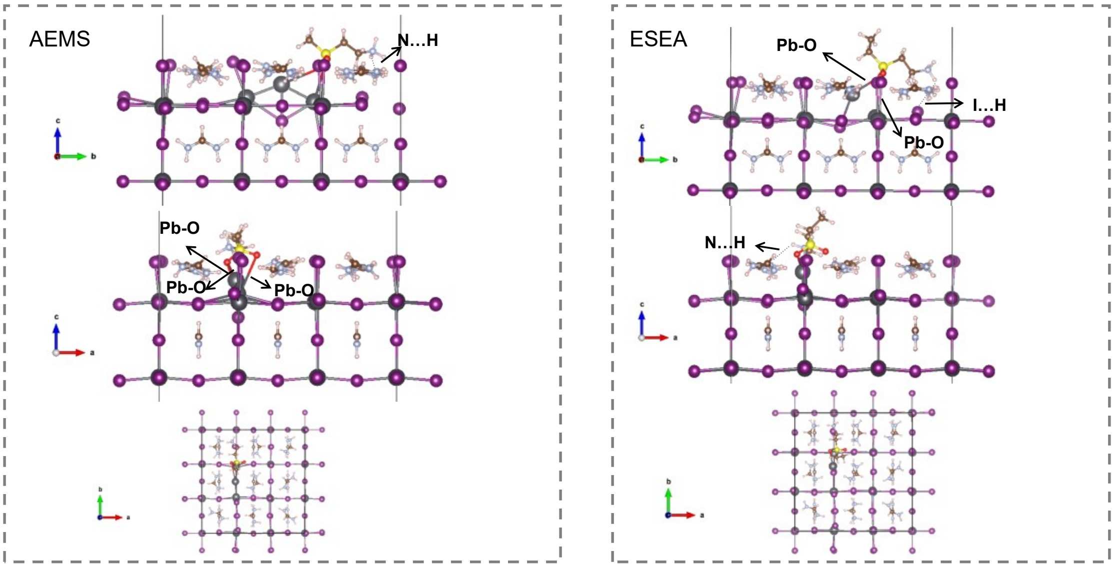

Fig. S3 The passivation effect of AEMS and ESEA ligands for $\mathrm{Pb_I}$ anti-defects. For each case, front, side, and top views are provided. The bonding configuration of AEMS involves Pb–O coordination bonds (sulfonyl group) and N···H hydrogen-bonding interactions (ammonium group). In contrast, the bonding configuration of ESEA consists of Pb–O coordination bonds (sulfonyl group) as well as N···H and H···I hydrogen-bonding interactions (ammonium group).

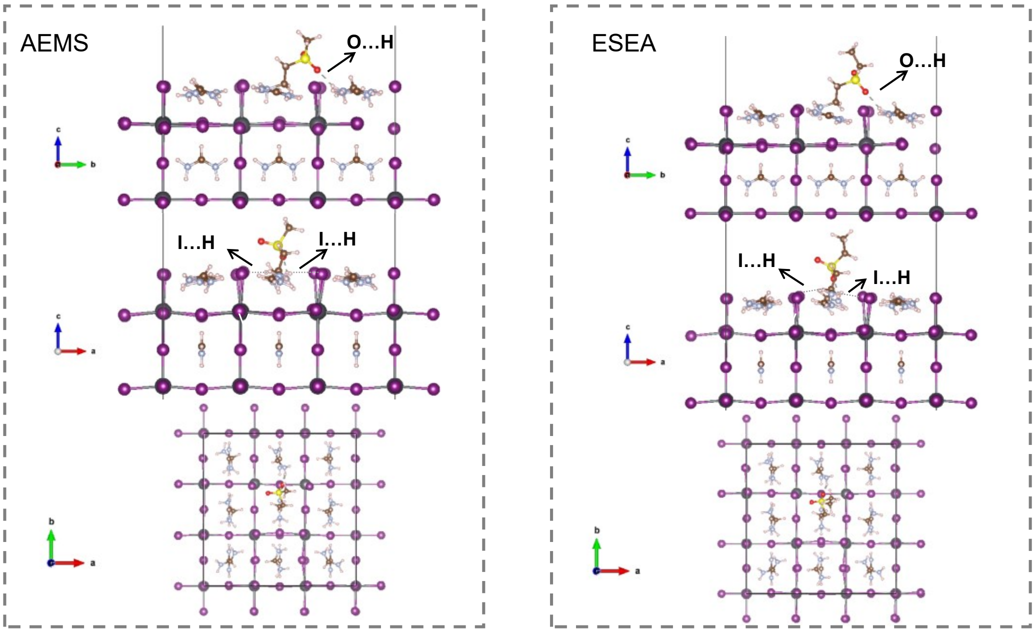

Fig. S4 The passivation effect of AEMS and ESEA ligands for V_{FA} defects. For each case, front, side, and top views are provided. Both AEMS and ESEA exhibit bonding configurations that involve O–H (sulfonyl group) and H···I hydrogen-bonding interactions (ammonium group).

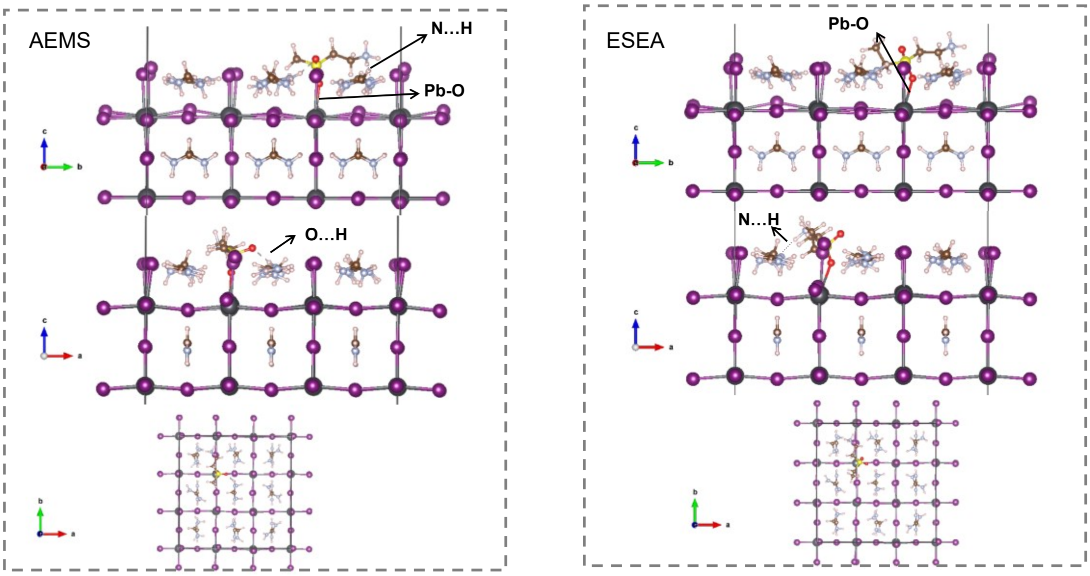

Fig. S5 The passivation effect of AEMS and ESEA ligands for V_I defects. For each case, front, side, and top views are provided. The bonding configuration of AEMS involves Pb–O coordination bonds (sulfonyl group), O–H (sulfonyl group), and N···H hydrogen-bonding interactions (ammonium group). In contrast, the bonding configuration of ESEA consists of Pb–O coordination bonds (sulfonyl group) and N···H hydrogen-bonding interactions (ammonium group).

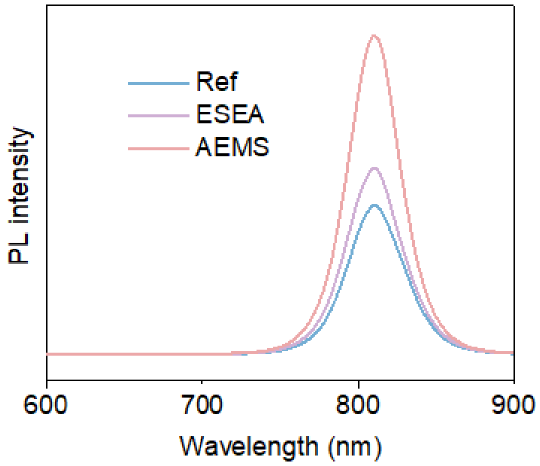

Fig. S6 Steady-state PL spectra of Ref, ESEA, and AEMS perovskite films.

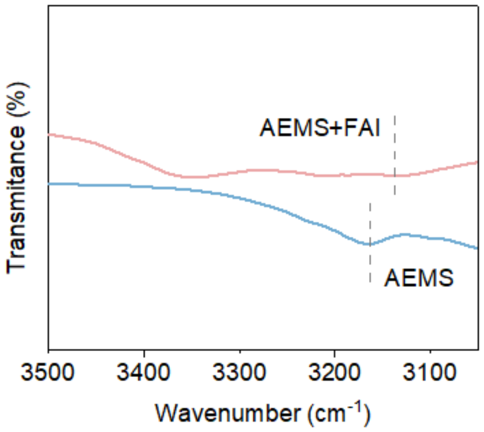

Fig. S7 FTIR spectra of AEMS and AEMS with FAI.

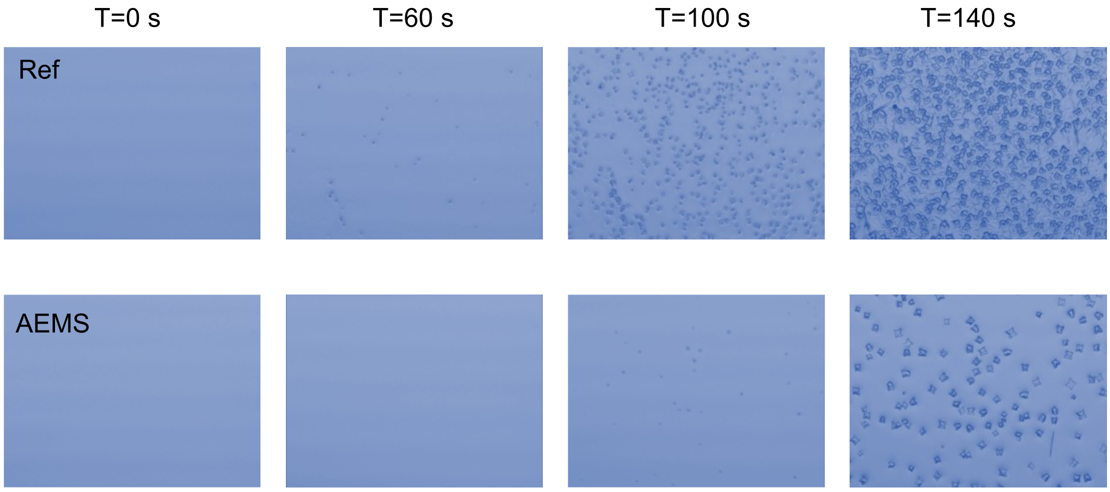

Fig. S8 Semi-in situ observation of perovskite precursor film morphology evolutions over time with an optical microscope with a 50 × objective lens.

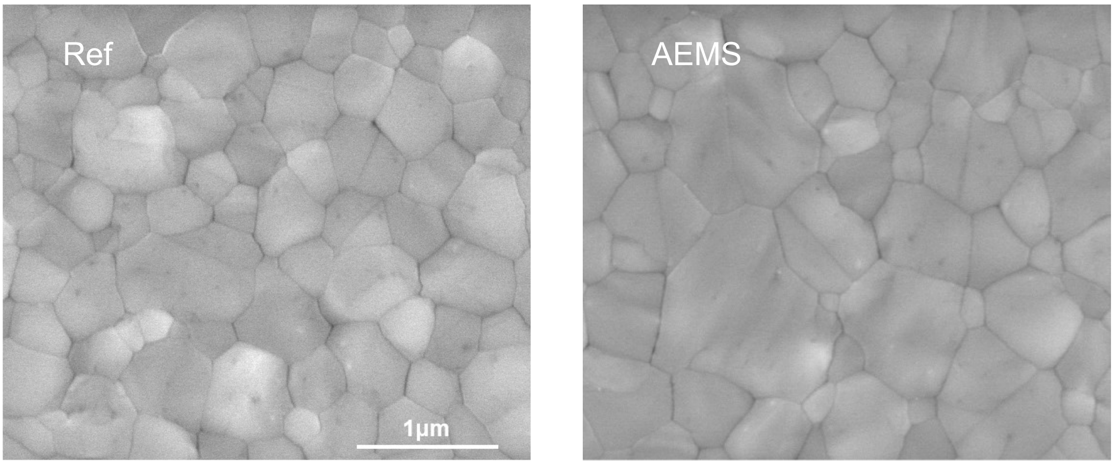

Fig. S9 SEM images of the top surfaces of Ref and AEMS perovskite films.

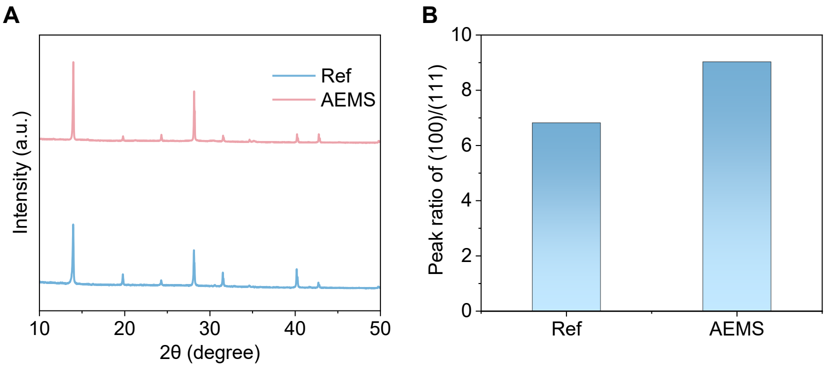

Fig. S10 Characterization of film crystallinity. (A) XRD measurements of Ref and the AEMS perovskite films. (B) The peak ratio relative to the (111) peak of each case.

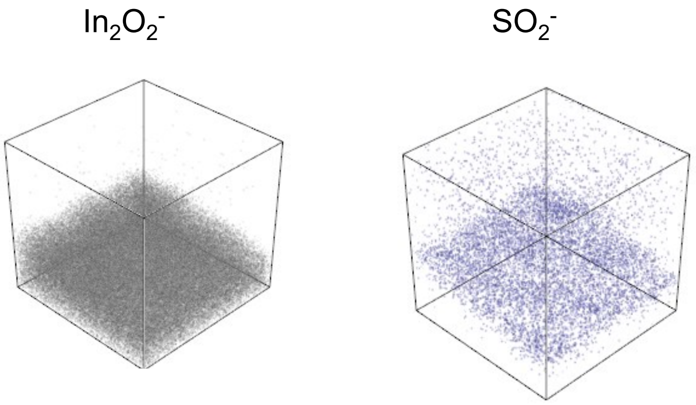

Fig. S11 3D element and group distributions for $In_2O_2^-$ and SO_2^- in the AEMS-based perovskite film. Here, the $In_2O_2^-$ signal originates from the elemental composition of the substrate (ITO), while the SO_2^- signal arises from the O=S=O functional group in AEMS. This result clearly indicates the accumulation of AEMS ligands at the bottom of the perovskite film.

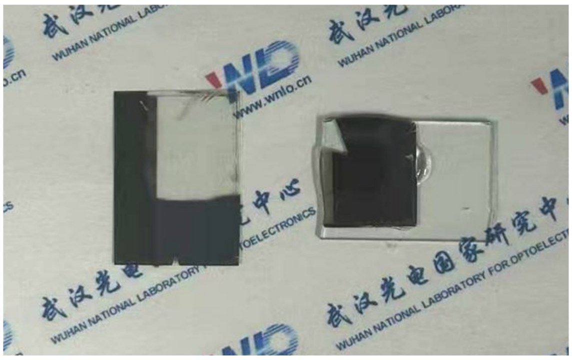

Fig. S12 Peel-off method for the bottom surfaces of perovskite films.

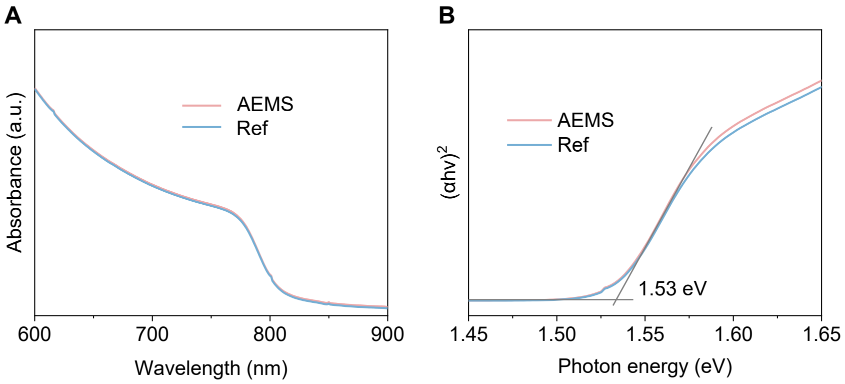

Fig. S13 Optical absorption characteristics of the films. (A) UV-vis absorption spectra of the Ref and AEMS-based perovskite films. (B) Tauc plot of the prepared perovskite films extracted from UV-vis absorption spectra.

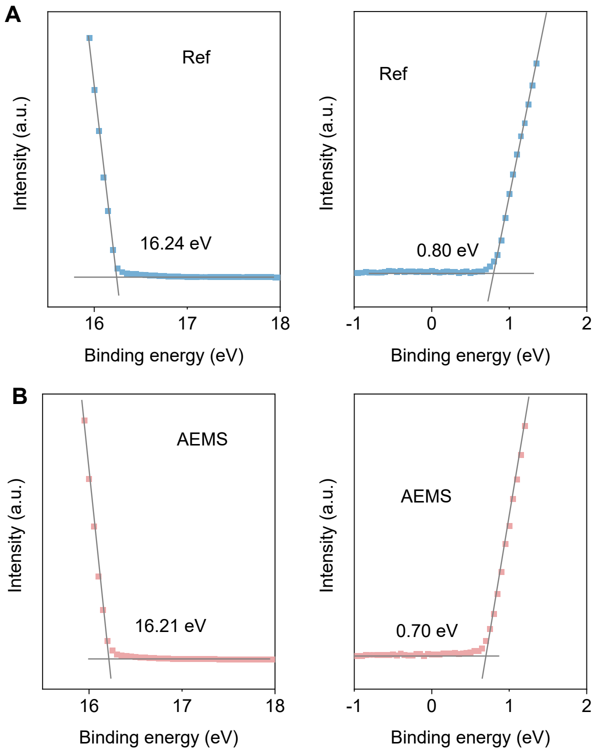

Fig. S14 Electronic structure of the perovskite films. UPS spectra of the (A) Ref and (B) AEMS-based perovskite films.

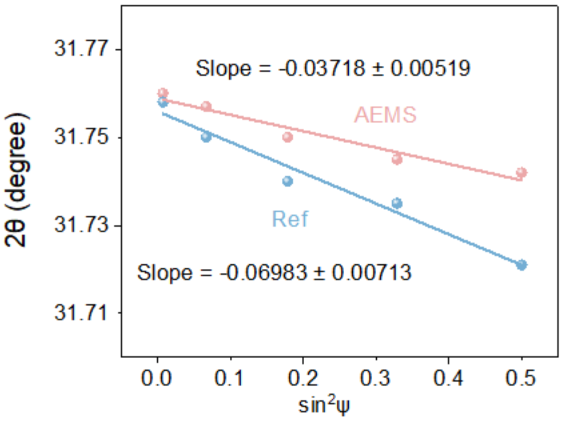

Fig. S15 2θ versus sin$^2\psi$ plots for the Ref and AEMS-based perovskite films.

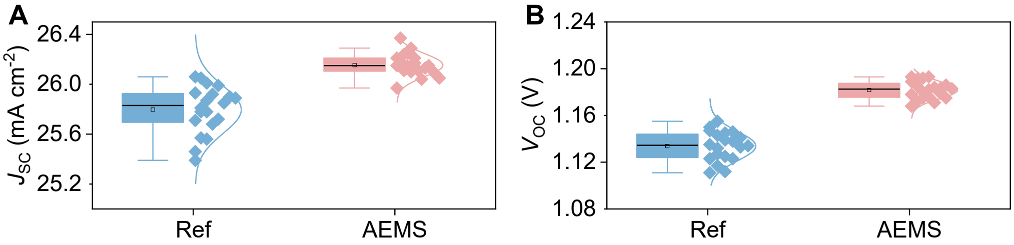

Fig. S16 Photovoltaic parameters (J_{SC} and V_{OC}) of devices with different ligands (20 devices for each type).

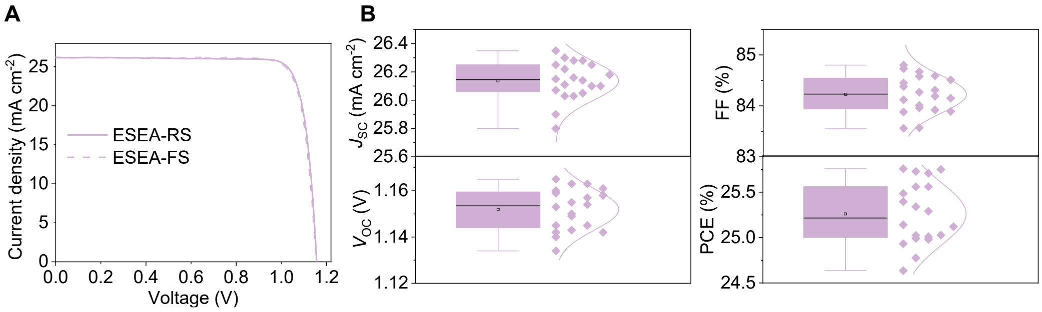

Fig. S17 Device performance based on ESEA-treated perovskite devices. (A) *J*–*V* curves of champion ESEA-treated devices under reverse and forward scans. (B) Photovoltaic parameters (J_{SC}, FF, V_{OC}, and PCE) of ESEA-treated devices (20 devices for each type).

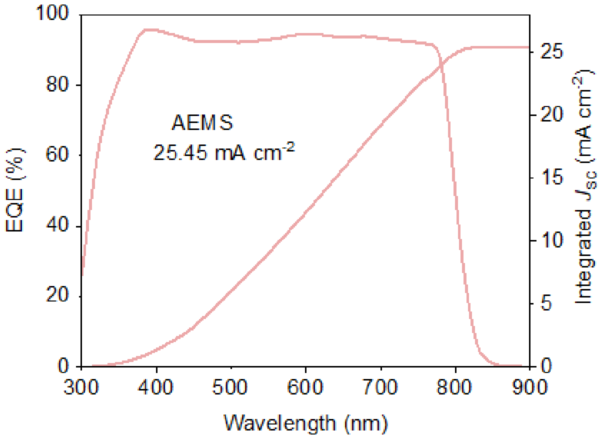

Fig. S18 EQE spectra and integrated J_{SC} values for the champion AEMS PSCs.

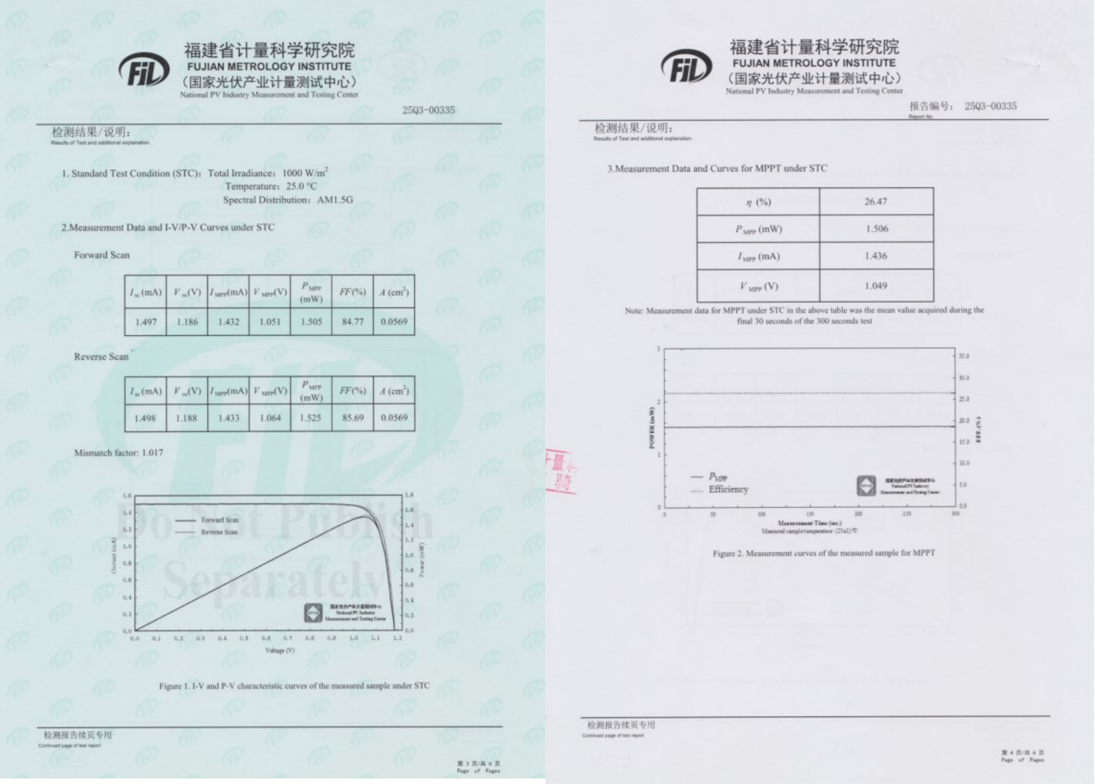

福建省计量科学研究院
FUJIAN METROLOGY INSTITUTE
（国家光伏产业计量测试中心）
National PV Industry Measurement and Testing Center

25Q3-00335

检测结果/说明：
Results of Test and additional explanation

1. Standard Test Condition (STC)：Total Irradiance：1000 W/m^2
Temperature：25.0 °C
Spectral Distribution：AM1.5G

2.Measurement Data and I-V/P-V Curves under STC

Forward Scan

I_{sc} (mA)	V_{oc}(V)	I_{MPP}(mA)	V_{MPP}(V)	P_{MPP} (mW)	FF(%)	A (cm^2)
1.497	1.186	1.432	1.051	1.505	84.77	0.0569

Reverse Scan

I_{sc} (mA)	V_{oc}(V)	I_{MPP}(mA)	V_{MPP}(V)	P_{MPP} (mW)	FF(%)	A (cm^2)
1.498	1.188	1.433	1.064	1.525	85.69	0.0569

Mismatch factor: 1.017

Figure 1. I-V and P-V characteristic curves of the measured sample under STC

检测报告续页专用
Continued page of test report

第 3 页/共 6 页
Page of Pages

福建省计量科学研究院
FUJIAN METROLOGY INSTITUTE
（国家光伏产业计量测试中心）
National PV Industry Measurement and Testing Center

报告编号：25Q3-00335
Report No.

检测结果/说明：
Results of Test and additional explanation

3.Measurement Data and Curves for MPPT under STC

η (%)	26.47
P_{MPP} (mW)	1.506
I_{MPP} (mA)	1.436
V_{MPP} (V)	1.049

Note: Measurement data for MPPT under STC in the above table was the mean value acquired during the final 30 seconds of the 300 seconds test

Figure 2. Measurement curves of the measured sample for MPPT

检测报告续页专用
Continued page of test report

第 4 页/共 6 页
Page of Pages

Fig. S19 Certified photovoltaic data of the inverted PSC based on AEMS strategy. The Chinese National PV Industry Measurement and Testing Center (NPVM) issued the report. The certified PCE is 26.80% from the reverse scan, and the stabilized PCE of 26.47% is determined from maximum-power-point tracking (MPPT) for 300 s.

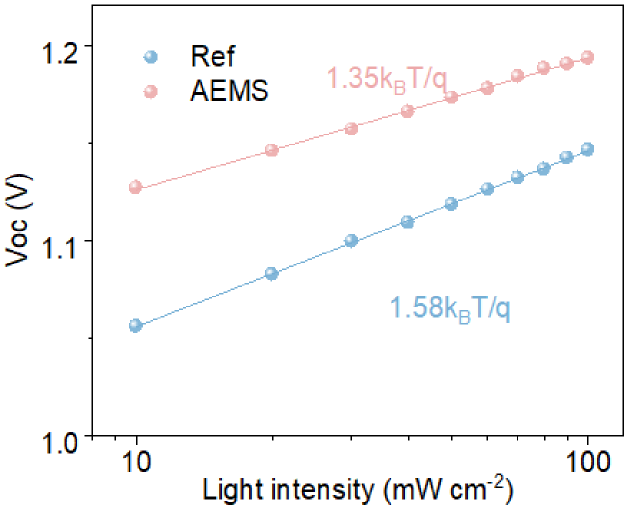

Fig. S20 Light intensity dependence of V_{OC} on the Ref and AEMS-based PSCs.

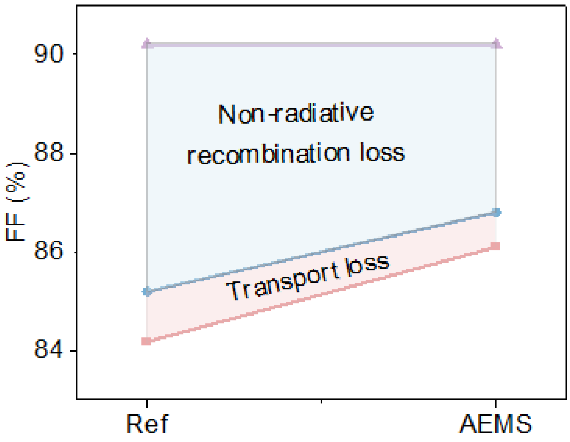

Fig. S21 Detailed FF loss analysis of the Ref and AEMS PSCs.

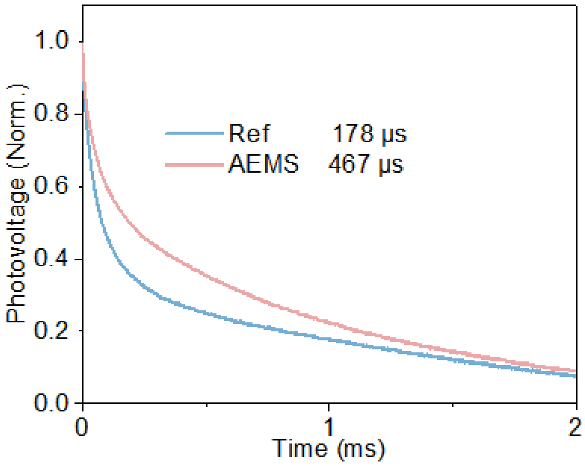

Fig. S22 Transient photovoltage (TPV) plots of the Ref and AEMS devices.

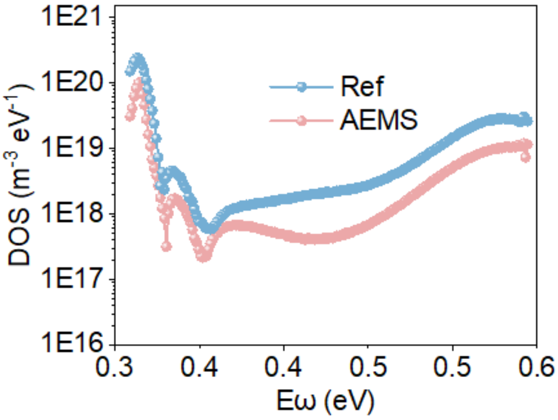

Fig. S23 Trap density of states (tDOS) plots of devices with and without AEMS ligand.

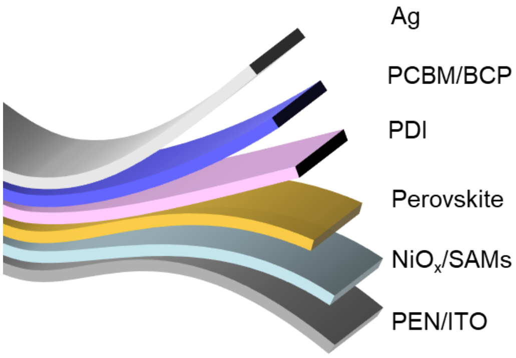

Fig. S24 Device configuration of inverted flexible PSCs.

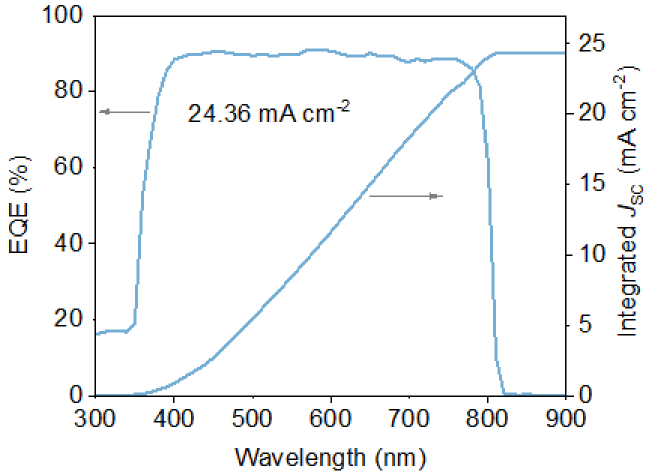

Fig. S25 EQE spectra and integrated J_{SC} values for the champion AEMS flexible PSCs.

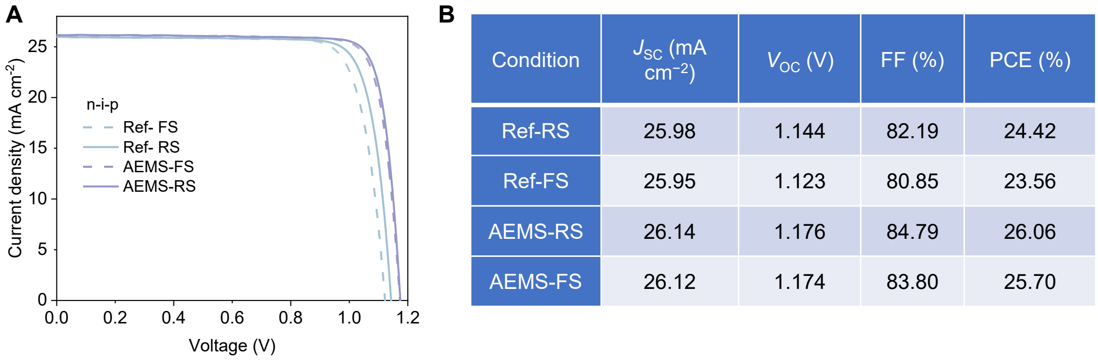

Condition	J_{SC} (mA cm^{-2})	V_{OC} (V)	FF (%)	PCE (%)
Ref-RS	25.98	1.144	82.19	24.42
Ref-FS	25.95	1.123	80.85	23.56
AEMS-RS	26.14	1.176	84.79	26.06
AEMS-FS	26.12	1.174	83.80	25.70

Fig. S26 Device performance based on AEMS-treated n-i-p perovskite devices. (A) *J*–*V* curves of champion Ref- and AEMS-treated devices under reverse and forward scans. (B) Photovoltaic parameters (J_{SC}, FF, V_{OC}, and PCE) of corresponding devices.

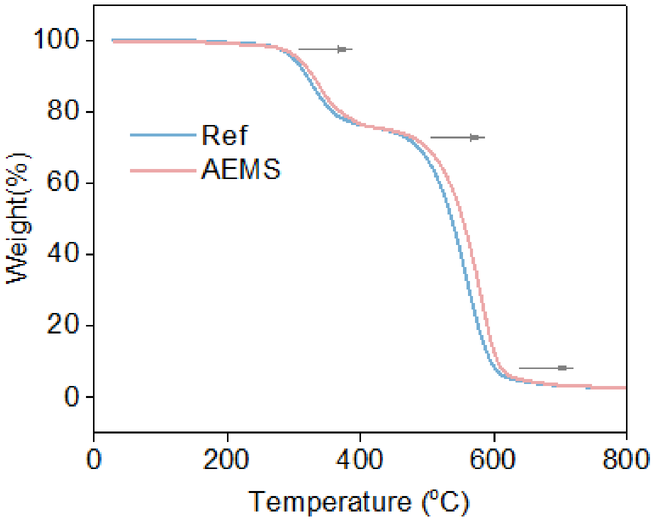

Fig. S27 Thermogravimetric analysis (TGA) of weight loss of Ref and AEMS-based perovskite films, respectively.

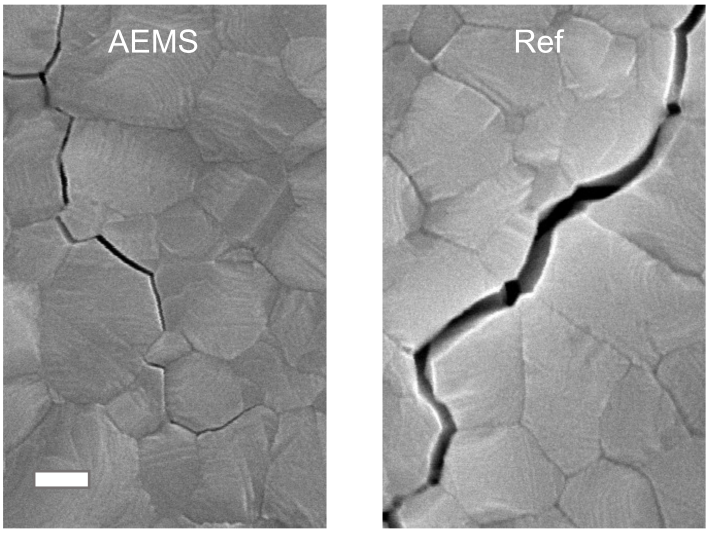

Fig. S28 Bottom surface morphology of perovskite films on flexible substrates. Bottom-view SEM images of the Ref and AEMS perovskite films after 6,000 bending cycles with a radius of 5 mm, Scale bars, 200 nm.

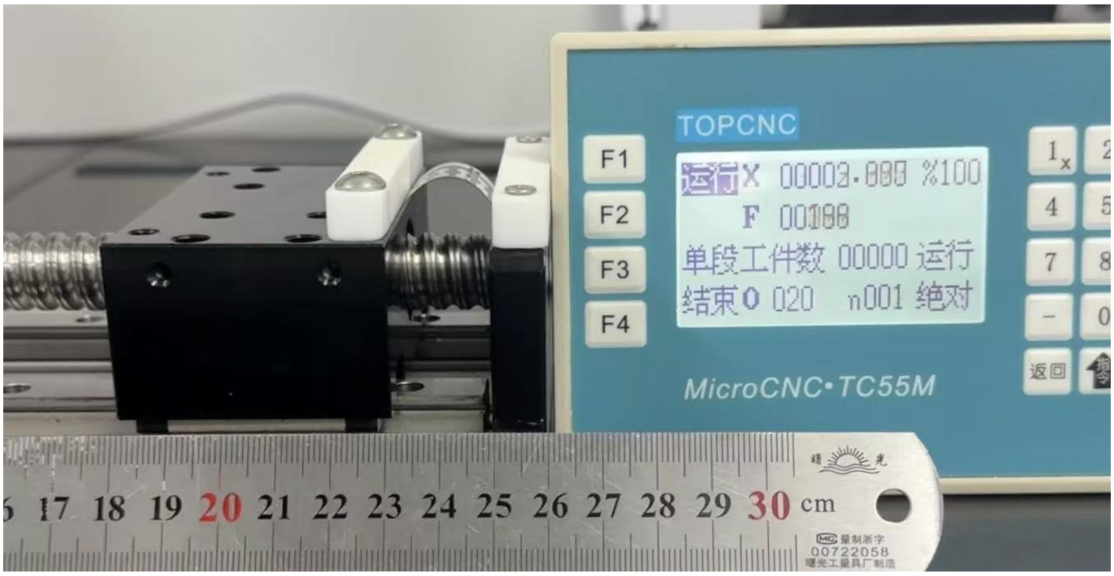

Fig. S29 Equipment for mechanical bending tests of flexible devices.

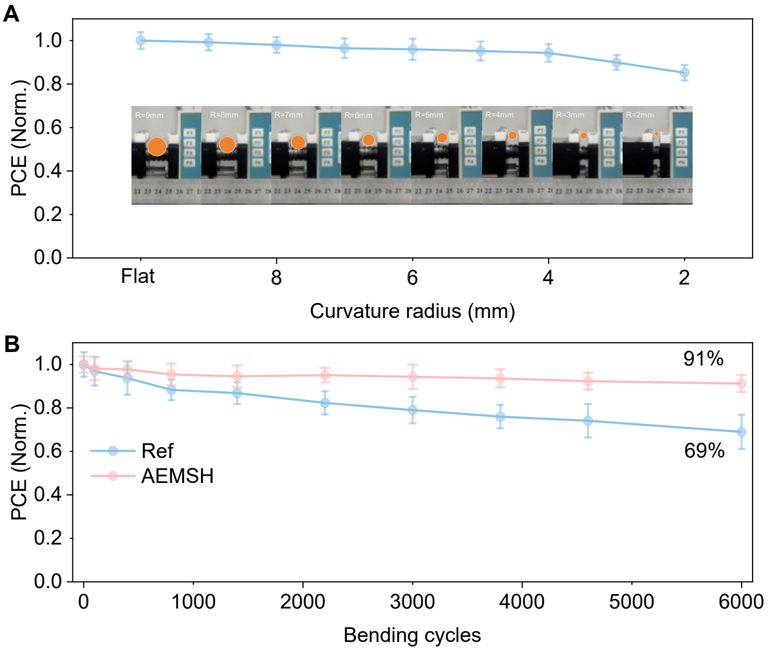

Fig. S30 Mechanical stability of the flexible PSCs. (A) PCE variations of AEMS-based flexible PSCs subjected to mechanical bending tests with curvature radii ranging from 9 mm to 2 mm (10 devices for each type). (B) Mechanical stability of the flexible PSCs versus bending cycles at a radius of 4 mm.

Table S1. The PL decay fitting parameters of Ref, ESEA, and AEMS perovskite films.

Samples	A_1	τ_1 (ns)	A_2	τ_2 (ns)	τ_{ave} (ns)
Ref	0.489	5.998	0.576	247.55	242.68
ESEA	0.376	111.09	0.380	665.82	587.22
AEMS	0.347	67.059	0.408	906.80	857.11

The average carrier lifetime (τ_{ave}) was calculated according to the equation:

$$\tau_{ave} = \frac{A_1\tau_1 + A_2\tau_2}{A_1 + A_2}$$

Table S2. Electronic parameters of the Ref and AEMS perovskite films extracted from UPS spectra.

Condition	E_{cutoff} (eV)	E_{onset} (eV)	VBM (eV)	Eg (eV)	CBM (eV)
Ref	16.24	0.80	−5.78	1.53	−4.25
AEMS	16.21	0.70	−5.71	1.53	−4.18

Table S3. Summary of PLQY and QFLS of the Ref and AEMS-based perovskite films with and without charge transport layers deposition.

Conditions		PLQY (%)	QFLS (eV)
PVK	Ref	9.3	1.216
	AEMS	13.2	1.225
HTL/PVK	Ref	3.23	1.189
	AEMS	9.16	1.216
PVK/ETL	Ref	4.45	1.197
	AEMS	9.04	1.215

Table S4. The detailed photovoltaic parameters of champion devices.

Condition	J_{SC} (mA cm^{-2})	V_{OC} (V)	FF (%)	PCE (%)
Ref-RS	25.93	1.150	84.18	25.10
Ref-FS	25.90	1.147	83.33	24.76
ESEA-RS	26.21	1.160	84.73	25.76
ESEA-FS	26.16	1.154	84.15	25.40
AEMS-RS	26.21	1.193	86.06	26.91
AEMS-FS	26.19	1.191	85.60	26.70

Table S5. Summary of representative certified *J-V* PCE >24% of inverted PSCs based on $FA_{1-x}Cs_xPbI_3$.

Ref.	V_{OC} (V)	J_{SC} (mA cm^{-2})	FF (%)	*J-V* PCE (%)
This work	**1.188**	**26.33**	**85.69**	**26.80**
Nat. Nanotechnol. 20, 772-778 (2025)[13]	1.173	25.51	84.70	25.33
Science 382, 1399-1404 (2023)[14]	1.183	26.23	81.20	25.20
Nat. Energy 8, 839-849 (2023)[1]	1.167	25.80	81.49	24.54
Nat. Energy 8, 946-955 (2023)[15]	1.173	25.69	81.63	24.60
Nature 624, 557-563 (2023)[16]	1.153	26.50	84.46	25.80
Nature 632, 536–542 (2024)[2]	1.192	26.47	84.11	26.54
Nat. Commun. 16, 1252 (2025)[17]	1.187	25.87	84.72	26.02

Table S6. Photovoltaic parameters of the AEMS-based champion PSMs (aperture area: 11.1 cm^2).

Scan direction	J_{SC} (mA cm^{-2})	V_{OC} (V)	FF (%)	PCE (%)
Reverse	4.80	5.918	81.80	23.24
Forward	4.80	5.913	80.75	22.92

References

1 R. Chen, J. Wang, Z. Liu, F. Ren, S. Liu, J. Zhou, H. Wang, X. Meng, Z. Zhang, X. Guan, W. Liang, P. A. Troshin, Y. Qi, L. Han and W. Chen, *Nat. Energy*, 2023, **8**, 839-849.

2 S. Liu, J. Li, W. Xiao, R. Chen, Z. Sun, Y. Zhang, X. Lei, S. Hu, M. Kober-Czerny, J. Wang, F. Ren, Q. Zhou, H. Raza, Y. Gao, Y. Ji, S. Li, H. Li, L. Qiu, W. Huang, Y. Zhao, B. Xu, Z. Liu, H. J. Snaith, N.-G. Park and W. Chen, *Nature*, 2024, **632**, 536-542.

3 Z. Ni, C. Bao, Y. Liu, Q. Jiang, W.-Q. Wu, S. Chen, X. Dai, B. Chen, B. Hartweg, Z. Yu, Z. Holman and J. Huang, *Science*, 2020, **367**, 1352-1358.

4 G. Kresse and J. Furthmüller, *Comput. Mater. Sci.*, 1996, **6**, 15-50.

5 Kresse and Furthmuller, *Phys. Rev. B*, 1996, **54**, 11169-11186.

6 P. E. Blöchl, *Phys. Rev. B*, 1994, **50**, 17953-17979.

7 J. P. Perdew, K. Burke and M. Ernzerhof, *Phys. Rev. Lett.*, 1996, **77**, 3865-3868.

8 J. P. Perdew and Y. Wang, *Phys. Rev. B*, 1992, **46**, 12947-12954.

9 S. Grimme, J. Antony, S. Ehrlich and H. Krieg, *J. Chem. Phys.*, 2010, **132**, 154104.

10 B. Delley, *J. Chem. Phys.*, 1990, **92**, 508-517.

11 B. Delley, *J. Chem. Phys.*, 2000, **113**, 7756-7764.

12 Y. Zhao and D. G. Truhlar, *J. Chem. Phys.*, 2006, **125**, 194101.

13 S. Fu, N. Sun, H. Chen, C. Liu, X. Wang, Y. Li, A. Abudulimu, Y. Xu, S. Ramakrishnan, C. Li, Y. Yang, H. Wan, Z. Huang, Y. Xian, Y. Yin, T. Zhu, H. Chen, A. Rahimi, M. M. Saeed, Y. Zhang, Q. Yu, D. S. Ginger, R. J. Ellingson, B. Chen, Z. Song, M. G. Kanatzidis, E. H. Sargent and Y. Yan, *Nat. Nanotechnol.*, 2025, **20**, 772-778.

14 S. Yu, Z. Xiong, H. Zhou, Q. Zhang, Z. Wang, F. Ma, Z. Qu, Y. Zhao, X. Chu, X. Zhang and J. You, *Science*, 2023, **382**, 1399-1404.

15 H. Li, C. Zhang, C. Gong, D. Zhang, H. Zhang, Q. Zhuang, X. Yu, S. Gong, X. Chen, J. Yang, X. Li, R. Li, J. Li, J. Zhou, H. Yang, Q. Lin, J. Chu, M. Grätzel, J. Chen and Z. Zang, *Nat. Energy*, 2023, **8**, 946-955.

16 Z. Liang, Y. Zhang, H. Xu, W. Chen, B. Liu, J. Zhang, H. Zhang, Z. Wang, D.-H. Kang, J. Zeng, X. Gao, Q. Wang, H. Hu, H. Zhou, X. Cai, X. Tian, P. Reiss, B. Xu, T. Kirchartz, Z. Xiao, S. Dai, N.-G. Park, J. Ye and X. Pan, *Nature*, 2023, **624**, 557-563.

17 Y. Peng, Y. Chen, J. Zhou, C. Luo, W. Tang, Y. Duan, Y. Wu and Q. Peng, *Nat. Commun.*, 2025, **16**, 1252.